ORIGINAL RESEARCH ARTICLE

Enhancement in the Mechanical Properties of Newly Developed Ceramic Reinforced Al-Based Syntactic Foams: Analysis of Microstructure, Mechanical Response, and Energy Absorption Properties

Kartheek S.M. Sonti, Suresh Kumar Reddy Narala, and S. Vincent

Traditional techniques for manufacturing aluminum matrix syntactic foams (AMSFs), such as stir casting and powder metallurgy procedures, may yield undesired pores. There is scope to study the energy absorption characteristics of AMSFs at varying strain rates. Comprehending these characteristics is essential for effectively using these materials in many industrial applications. This study fills the gap by employing a novel method, such as hot compaction, to achieve density close to theoretical calculations. The impact of ceramic particles and volume fraction on AMSFs is studied under uniaxial compression loading at varying strain rates (1-2700 s^{-1}). Also, deformation responses of AMSFs were observed using high-speed imaging for high-strain rate (HRS) tests. The stress–strain response indicates a positive shift in strain during dynamic loading and the maximum energy absorption properties achieved up to 72.34 and 78.92% for low- and high-strain rates, respectively. Further, the matrix failure is contributing to the hardening and deformation behavior at high-strain rates, offering valuable insights into the AMSF performance under different loading situations.

1. Introduction

Research on aluminum matrix syntactic foams (AMSFs), including ceramic hollow microparticles embedded in a metal matrix, has grown to decrease density and improve mechanical and acoustic characteristics. This lightweight material has attracted considerable interest in the automotive, aerospace, and marine sectors because of its low density, prolonged plateau region, and toughness under quasi-static loading (Ref 1-6). However, modern engineering constructions must exhibit exceptional performance when subjected to dynamic loading in addition to static loading.

Quasi-static research in the literature has examined AMSFs, emphasizing synthesis techniques (Ref 7-10), the effect of hollow particle size, and volume fraction (Ref 8, 11, 12), and loading in various environmental circumstances. Research on utilizing the liquid method to create syntactic foams has been ongoing for many years. Gupta et al. examined the mechanical characteristics of glass-based syntactic foams and documented a peak value of 27.8 MPa achieved by the liquid approach (Ref 13). This technology has been adapted to resolve the problems identified in the liquid pathways, such as undesired pores and inclusions in the matrix. Pen et al. reported the quasi-static compression behavior of the $Al-Al_2O_3$ SFs produced using the gravity casting technique. A maximum energy absorption capacity of 48.92 MJ/m^3 was reported (Ref 7). Further, the AMSFs are made using the pressure infiltration technique by Zhang and Zhao to improve the distribution of the hollow particles. The SFs are further analyzed at different strain rate conditions (Ref 9).

Another study found that small hollow sphere-filled SFs have high compressive strength, which makes them appropriate for structural purposes. In contrast, bimodal and large hollow spheres filled with SFs are ideal for energy absorption due to their lower stress levels and potential for increased energy absorption through longer damping routes and constrained deformation (Ref 14). Zhang and Zhao presented a detailed analysis of the monotonous and cyclic loading on AMSFs. In this work, the densification strain is significantly influenced by the volume fraction of the hollow particles in monotonous loading (Ref 15). The hardening rate and the energy absorption are studied to understand the effect of particle types and size, processing techniques, and loading conditions in porous materials. Xia et al. reported Al-Si foam's energy absorption and hardening rate properties concerning different space holders (Ref 16).

Comprehending the dynamic characteristics of cellular materials is crucial for substituting traditional materials in the automotive and aerospace sectors. Alvandi-Tabrizi and Rabiei

Kartheek S.M. Sonti, Center of Excellence, Materials Technology, Mahindra and Mahindra, Chennai 603004, India; and Department of Mechanical Engineering, BITS Pilani, Hyderabad Campus, Hyderabad 500078, India; **Suresh Kumar Reddy Narala**, Department of Mechanical Engineering, BITS Pilani, Hyderabad Campus, Hyderabad 500078, India; and **S. Vincent**, Department of Mechanical Engineering, BITS Pilani Dubai Campus, Dubai 345055, UAE. Contact e-mail: nskreddy@hyderabad.bits-pilani.ac.in.

researched composite metal foam, which shows enhanced mechanical characteristics such as elastic modulus, strength, and energy absorption when subjected to high-speed impacts as opposed to quasi-static loading conditions. This enhancement is attributed to the effects of trapped air and microinertial forces within the foam's structure, with impact speed playing a crucial role in amplifying these effects. At the same time, sample size does not directly affect dynamic behavior as long as specific cell density criteria are met to avoid edge effects (Ref 17). Balch et al. performed dynamic compression studies at 2300 s^{-1} on aluminum-ceramic microspheres with a peak stress of 248 MPa. The cenosphere particles significantly contribute to the stiffness of the syntactic foams during dynamic loadings. Fan et al. predicted the dynamic compressive strength of polymer SFs reinforced with different cenosphere sizes (Ref 18). Another study on the effect of particle size on the dynamic response was reported by Geol et al., which showed enhanced mechanical strength with different percentages of the cenospheres introduced in an aluminum matrix (Ref 19). The matrix and reinforcement of the samples are examined under micro-CT tomography (Ref 20). In another study, silicon carbide-based hollow particles induced SFs with a 1.819 g/cm^3 density showed a maximum compressive strength of 181 MPa (Ref 21). The various combinations of matrix and reinforcements yield at least a 10-30% rise in peak stress observed under dynamic compression (Ref 22-24).

The synthesis techniques adopted to produce the SFs need constant improvement to enhance the mechanical properties and energy absorption. Previous studies indicate the necessity of comprehending alumina-reinforced aluminum-based syntactic foams under various stress circumstances. Also, the effect of alumina hollow particles under various loading conditions and their deformation response should be discussed in detail. This work attempts to produce the AMSFs using newly adopted techniques such as hot compactions. The study examines the impact of varying the strain rates on hollow particles' volume percentage and diameter. The low- and high-strain rate properties are captured to study the effect of brittle alumina particles in a soft matrix material such as aluminum. The hardening behavior and energy absorption properties of the AMSFs are studied for samples tested at 2700 s^{-1} and compared against the low-strain rate (1 s^{-1}) results. The deformed behavior is examined using DIC, and samples are tested to understand the deformed behavior. These studies on Al-Al$_2$O$_3$ syntactic foams at high-strain rates help understand relative density's effect and material response under various loading conditions.

2. Materials and Methods

2.1 Synthesis of AMSFs

The AMSFs is hot compaction, which is done by loading the powder mixture of matrix and alumina particles in a die and producing AMSFs in a single step. The raw materials aluminum powder and alumina hollow particles are procured from SRL Pvt. Ltd. and KD Refractories Co. Ltd., respectively. The material composition details are alumina hollow particles—Al$_2$O$_3$ $\geq$ 99, SiO$_2$ $\leq$ 0.18, Na$_2$O $\leq$ 0.15, Fe$_2$O$_3$ $\leq$ 0.15, and Al-99.88%. The as-received hollow particles are segregated into three average particle sizes (250, 500, and 750 μm) for further processing, as shown in Fig. 1. Later, the
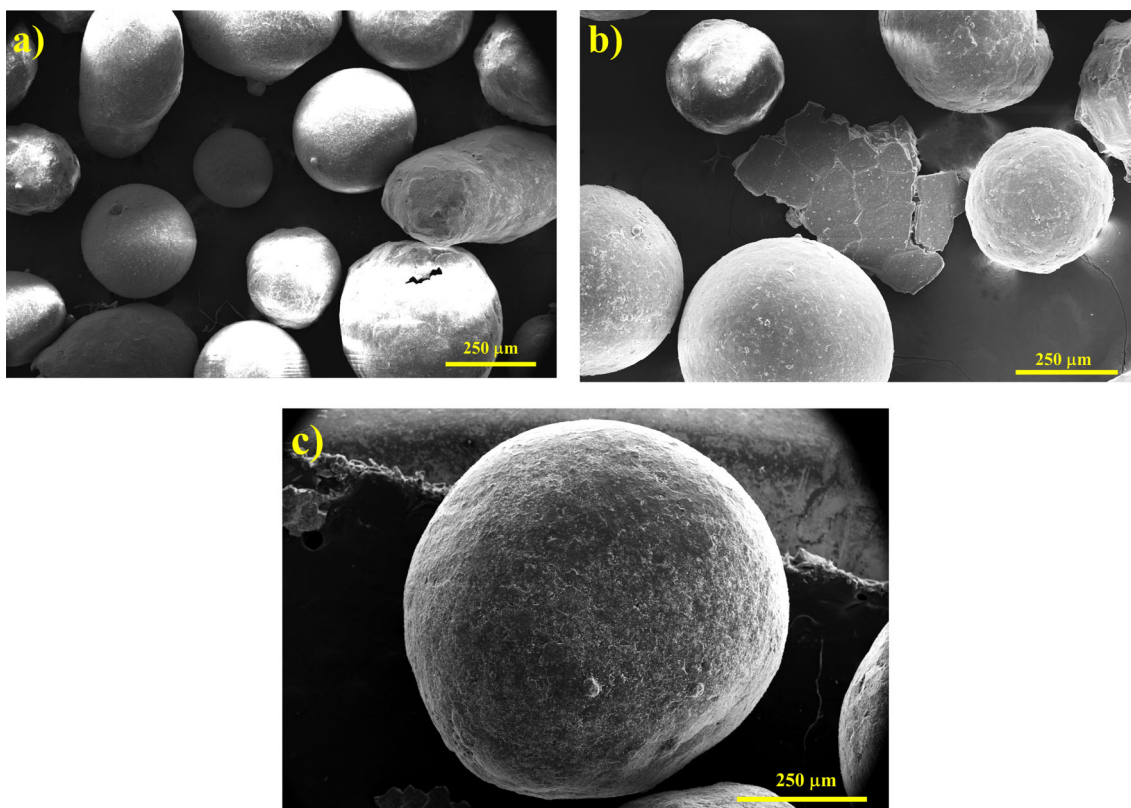

Fig. 1 As-received scanning electron images of alumina hollow particles of different sizes: (a) 250 mm, (b) 500 mm, and (c) 750 mm

aluminum powder (particle size < 50 μm) is mixed with the hollow particles as per the volume fraction (10, 20, and 30%) using a vibratory mixing jar. After mixing for 15 min for each batch, the composite mixture is collected and transferred to a stainless-steel die assembly. The entire assembly is kept under the heating chamber attached to the compression testing machine. The entire powder die assembly is heated to 450 °C of the matrix material with a heating rate of 8 °C per minute. Throughout this process, three thermocouples are connected directly to the outside surface of the die to monitor the temperatures. After reaching the set (450 °C) temperature, the uniaxial load is applied up to 60 MPa for 10-min holding time. A detailed illustration of the synthesis technique and heating, the loading sequence adopted, and the produced sample is shown in Fig. 2(a), (b), and (c). Later, the samples are cooled in atmospheric conditions, holding the load applied till the

assembly reaches room temperature. Nine samples of each condition are prepared by varying the volume fraction (10, 20, and 30%) and particle size (250, 500, and 750 μm). The corresponding sample ID details are provided in Table 1.

2.2 Microstructure and Density

The processed samples are examined using the freeze-fracture method to understand the distribution of the hollow particles inside the matrix. This method is discussed in our earlier works (Ref 2, 11). The surface of the samples and particles is examined using field emission scanning electron microscopy (FE-SEM) instrument. Later, the theoretical density of the AMSFs is obtained using the following equation:

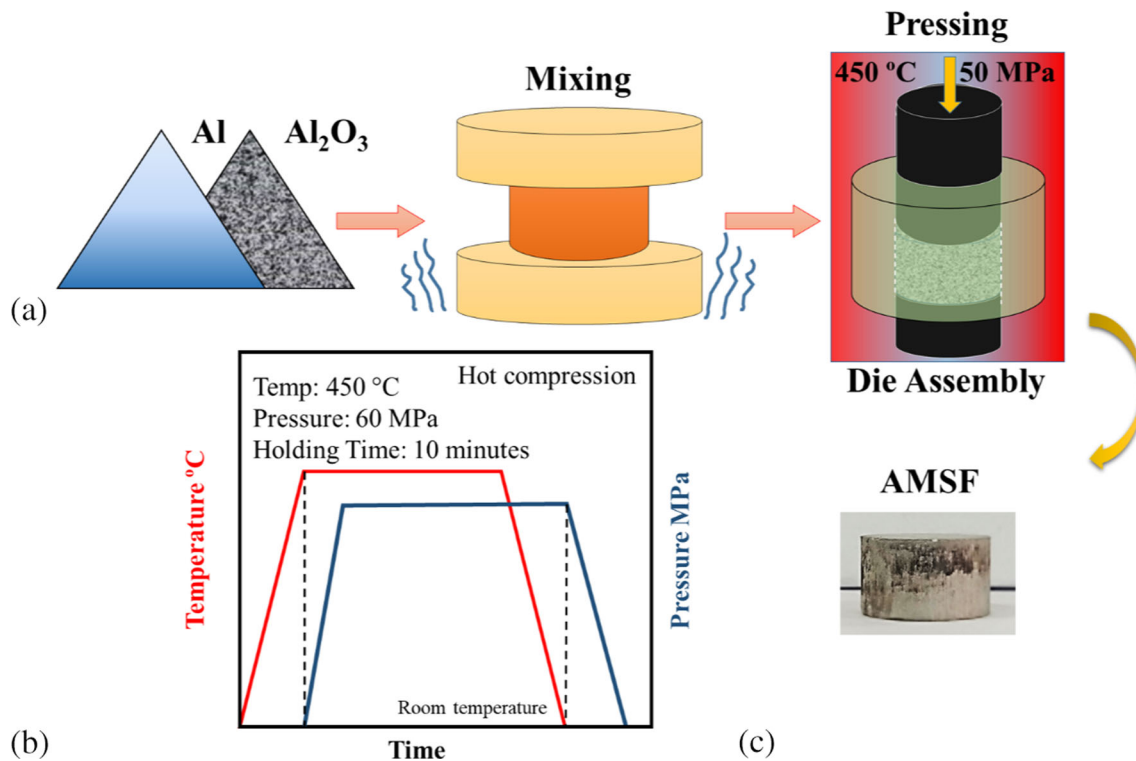$$\rho_T = (\rho_{HP} V_f) + \rho_m (1 - V_f) \qquad \text{(Eq 1)}$$

Fig. 2 (a) Schematic of hot compression technique adopted to produce AMSFs, (b) heating and compression sequence adopted, and (c) produced AMSF

Table 1 Experimental density and theoretical density of syntactic foam materials

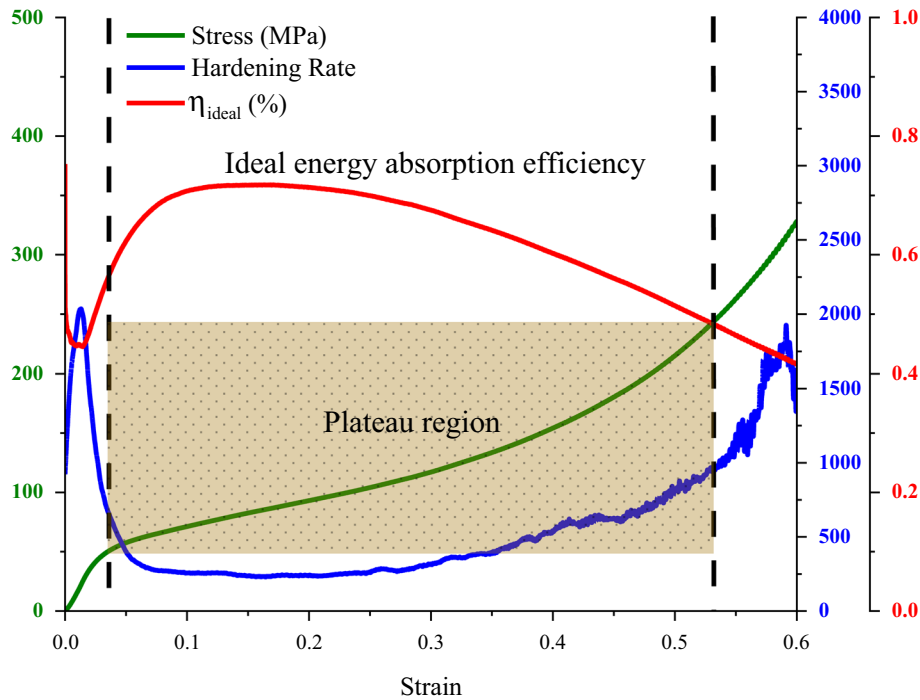| Sample ID	Volume fraction	Average particle size, mm	Hollow particle density, g/cm³	Theoretical density, g/cm³	Experimental density, g/cm³	Percentage deviation in the density	Relative density
#1	10	250	0.71	2.51	2.52	0.40	0.93
#2	20	250	0.71	2.31	2.30	0.43	0.85
#3	30	250	0.71	2.11	2.17	2.76	0.8
#4	10	500	0.66	2.5	2.49	0.40	0.92
#5	20	500	0.66	2.30	2.28	0.88	0.84
#6	30	500	0.66	2.09	2.11	0.95	0.78
#7	10	750	0.51	2.49	2.47	0.81	0.91
#8	20	750	0.51	2.27	2.25	0.89	0.83
#9	30	750	0.51	2.05	2.09	1.91	0.77

Fig. 3 Typical stress–strain, hardening rate curve, and energy absorption efficiency

The subscripts T, HP, and *m* denote densities of AMSFs, hollow particles, and matrix. Further, using the Mettler Toledo density kit, the experimental density of the AMSFs was measured. The average density data reported in this study are obtained from five repetitions of different samples.

2.3 Mechanical Studies

2.3.1 Quasi-Static Compression. To probe the deformation behavior of AMSFs and to understand the role of particle size and volume fraction, compression studies are performed on nine different samples at different strain rates. The quasi-static (1 s^{-1} strain rate) mechanical studies are conducted using Zwick Roell Z100 of load cell capacity 5 kN at room temperature. Before testing the samples, the top and bottom faces of the cylindrical samples are polished and lubricated to avoid friction between the plates and samples. The initial dimensions of the samples are recorded. Later, the stress versus strain data are obtained from the system-generated load versus displacement curves. The sample dimensions are 13 mm in diameter and 8 mm in height for all the test conditions.

2.3.2 Dynamic Compression. The high-strain rate studies are performed on the split Hopkinson pressure bar (SHPB) instrument at strain rates 900, 1800, and 2700 s^{-1} at room temperature. The SHPB instrument comprises two Al7075 alloyed bars of 2000 mm length and 28 mm diameter each. A projectile of similar material and cross-sectional dimensions is selected using a compressed air gun to propel at different velocities. The projectile hit the incident bar at the desired speed during the test. The signal transmitting in the incident bar is reflected at the interface of the specimen and incident bar. The remaining signal is transmitted through the specimen (which induces plastic deformation) and later into the transmitted bar in the form of the transmitted signal. The strain

gauge captures the impact loading caused due to striking from the bar. The instantaneous amplitude data from reflected and transmitted bars are later analyzed to attain the stress–strain data of individual samples. A representative strain gauge signal data and strain versus strain rate plot for 2700 s^{-1} are shown in Fig. 15 in Appendix. The phantom camera recorded the deformation process during the high-strain rate testing. Later, the DIC analysis was performed using open source Ncorr, a 2D image correlation software in MATLAB, to analyze the discrete images to develop a correlation between the deformed and undeformed samples. Further details on construction and equations to evaluate the material properties are discussed elsewhere (Ref 1, 25-27).

2.3.3 Energy Absorption Properties. In this work, the performance of the AMSFs is explored in three directions: stress–strain curve, hardening rate, and energy absorption efficiencies for samples tested at different rates. The information on energy absorption (EA) and specific energy absorption (SEA) properties of a material is crucial in selecting materials for structural applications. The EA information is obtained by measuring the area under the stress–strain curve (Ref. Eq 3) up to the maximum strain. Similarly, the SEA quantifies a material's energy absorption per unit mass. The SEA is usually measured by normalizing the EA with the density of the material.

The schematic of the model stress–strain data and its properties are shown in Fig. 3. The hardening rate of a material is studied by taking the derivative of the stress–strain data. The ideal energy absorption efficiency (I-EAE) data can be measured by normalizing the EA using the product of corresponding stress–strain values (Ref 16, 28-30).

$$\text{HR} = \frac{\int_0^\varepsilon \sigma \text{d}\varepsilon}{\sigma \varepsilon} \qquad \text{(Eq 2)}$$

$$EA = \int \sigma \mathrm{d}\varepsilon \qquad \text{(Eq 3)}$$

$$SEA = \frac{EA}{\rho}$$
$$I - EAE = \frac{EA}{\sigma\varepsilon} \qquad \text{(Eq 4)}$$

where ρ, σ, and ε are the density, stress, and strain data of AMSFs

3. Experimental Results

3.1 Microstructure and Density of AMSFs

Figure 4(A), (B), and (C) shows representative micrographs of three different sizes (250, 500, and 750 μm) of AMSFs. It is observed that the particles are firmly attached to the matrix materials post-freeze-fracture, particularly for low particle size samples with no evidence of undesired pours in the matrix. The response may be attributed to the processing technique. As the particle size increases, particle fractures. Also, the particles (750 μm) escape, leaving a void in the matrix, as shown in Fig. 4, represented by a red pointer. The theoretical, experimental, and corresponding relative density of all the samples are shown in Table 1. The relative density of the SF is measured by normalizing with the density of the matrix material (2.71 g/cm^3). It is observed that with an increase in the size of the hollow particle, the density of the particle decreases. This phenomenon may contribute to the density variation for different volume fractions of the SF materials. As the particle size increases, the volume fraction increases, and the density of the syntactic foam decreases. The produced SFs show little deviation from the theoretical density and indicate that controlled porosity is achieved. This can be attributed to the processing technique adopted.

3.2 Compressive Studies

In earlier studies, some SFs showed better energy absorption properties under compression low-strain rates (0.001 s^{-1}) (Ref 2, 4, 21). However, the performance of high-strain rates is seldom discussed for aluminum alumina systems as a function of size and volume fractions. Further sections discuss the quasi-static and dynamic performance of AMSFs and corresponding energy absorption efficiencies under different strain rates.

Figure 5(a), (b), (c), (d), (e), (f), (g), (h), and (i) displays the experimental stress–strain data of AMSFs at different strain rates. In Fig. 5, the volume fraction of the hollow sphere size is changed along the columns, and along rows, the size of the alumina hollow spheres is increased. In the linear elastic region, the deformation of AMSFs followed the same trend irrespective of the strain rate without significant deviation. Figure 5 also depicts the notable change in the yield point concerning the change in the strain rate. The stress–strain data followed a smooth transition from linear elastic to plastic regions in all studies without stress drops. The hollow particles tend to fracture during the plateau region, and the pores inside the matrix may be filled. However, this behavior does not significantly affect the stress values during the deformation, resulting in the material's hardening behavior. The maximum
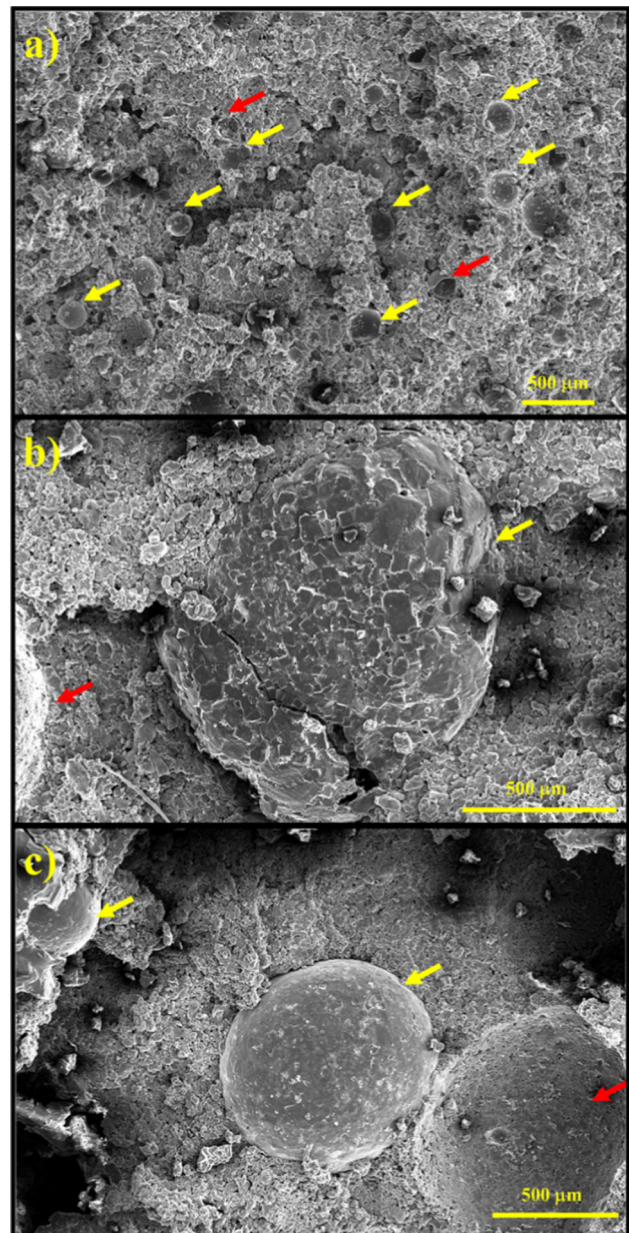

Fig. 4 Representative freeze fractures of 10% volume fraction of AMSFs are shown for (A) 250 mm, (B) 500 mm, and (C) 750 mm diameters

stress values at low and high strains are 184 and 288 MPa, respectively, at 0.45 strain. This hardening behavior is explored in detail later. Further, the slope of the curve follows a trend based on the hollow particles' size, volume fraction, and strain rate at which the samples are tested.

The deformation curves of the samples tested at higher strain rates showed a similar trend to the quasi-static tests up to the densification region. The typical strain observed in the samples corresponding to the deformation rate falls between 10-20% for 900 s^{-1} and 20-30% for 1800 s^{-1}. At a maximum strain rate of 2700 s^{-1}, the AMSFs deformed up to 40-50% strain. This behavior indicates early densification of the AMSFs compared to quasi-static deformation, irrespective of size and volume fractions.
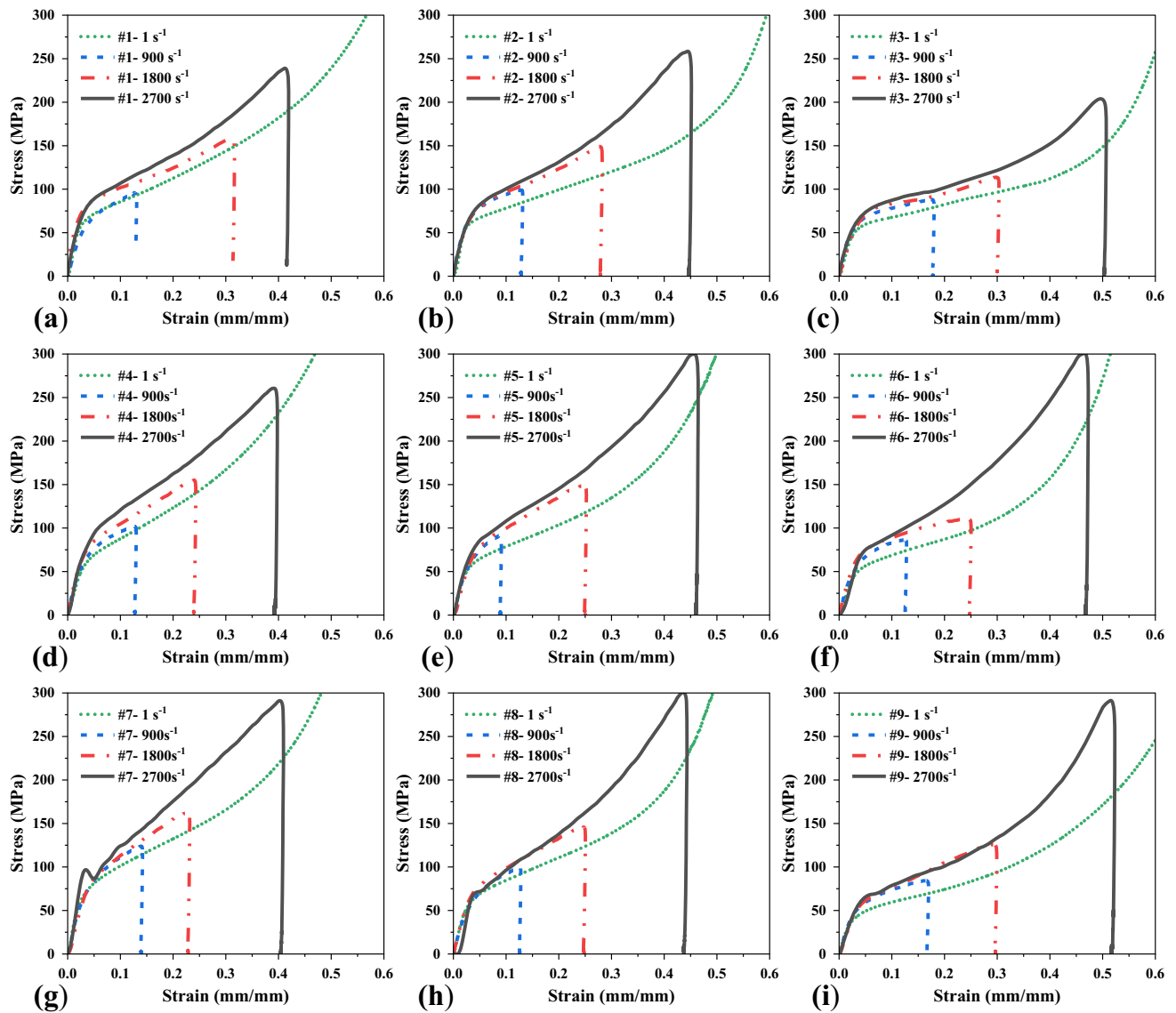
Fig. 5 Compressive stress–strain data of AMSFs at different strain rates of different sample IDs (a) #1, (b) #2, (c) #3, (d) #4, (e) #5, (f) #6, (g) #7, (h) #8, and (i) #9

The yield strength data measured are considered at 0.2% offset to the linear region of the stress–strain curve, and the average plateau stress values for all the samples are shown in Fig. 6. The yield stress values have followed an increasing trend with a rise in strain rate. This behavior is similar across different particle sizes. However, in samples tested at a particular strain rate (for example, at 2700 s^{-1} strain rate), there is a drop in the yield stress values with an increase in the volume fraction and particle size. The AMSFs exhibit the maximum yield strength of 151.62 and 196.39 MPa tested at 1 and 2700 s^{-1} strain rates, respectively. Figure 6(a), (b), and (c) also suggests that the overall yield strength of AMSFs decreases with a decrease in relative density, typically between 0.77 and 0.93.

Similarly, the average plateau stress values of AMSFs, as shown in Fig. 6(d), (e), and (f), followed a decreasing trend with an increase in the volume fraction and particle size. The AMSFs tested at medium strain rates (900 and 1800 s^{-1}) show minor deformation. This results in low plateau stress values.

Statistically, the maximum deviation in the average plateau stress value among the low- and high-strain rates is observed at low-volume fractions. However, as shown in Fig. 5, the maximum strain obtained for lower volume fractions has shown early densification and low strains with larger particles. This behavior needs to be further studied to understand the overall effect of the particle size and volume fraction on the mechanical response at various strain rates.

After deformation, the cross-sectional image of the samples using SEM and their respective EDX spectrum is obtained. A representative image and EDX spectrum of sample #3 tested at a high-strain rate are shown in Fig. 7. The arrows indicate the compression direction of the sample tested. Figure 7(a), (b), and (c) shows the particle deformation pattern of samples tested at three strain rates (900, 1800, and 2700 s^{-1}), respectively. The particles tested at 900 s^{-1} show fractured particles without complete failure of the shell structure of hollow particles.

Similarly, the residual amount of hollow particles is observed in the sample tested at 1800 s^{-1}. However, at higher
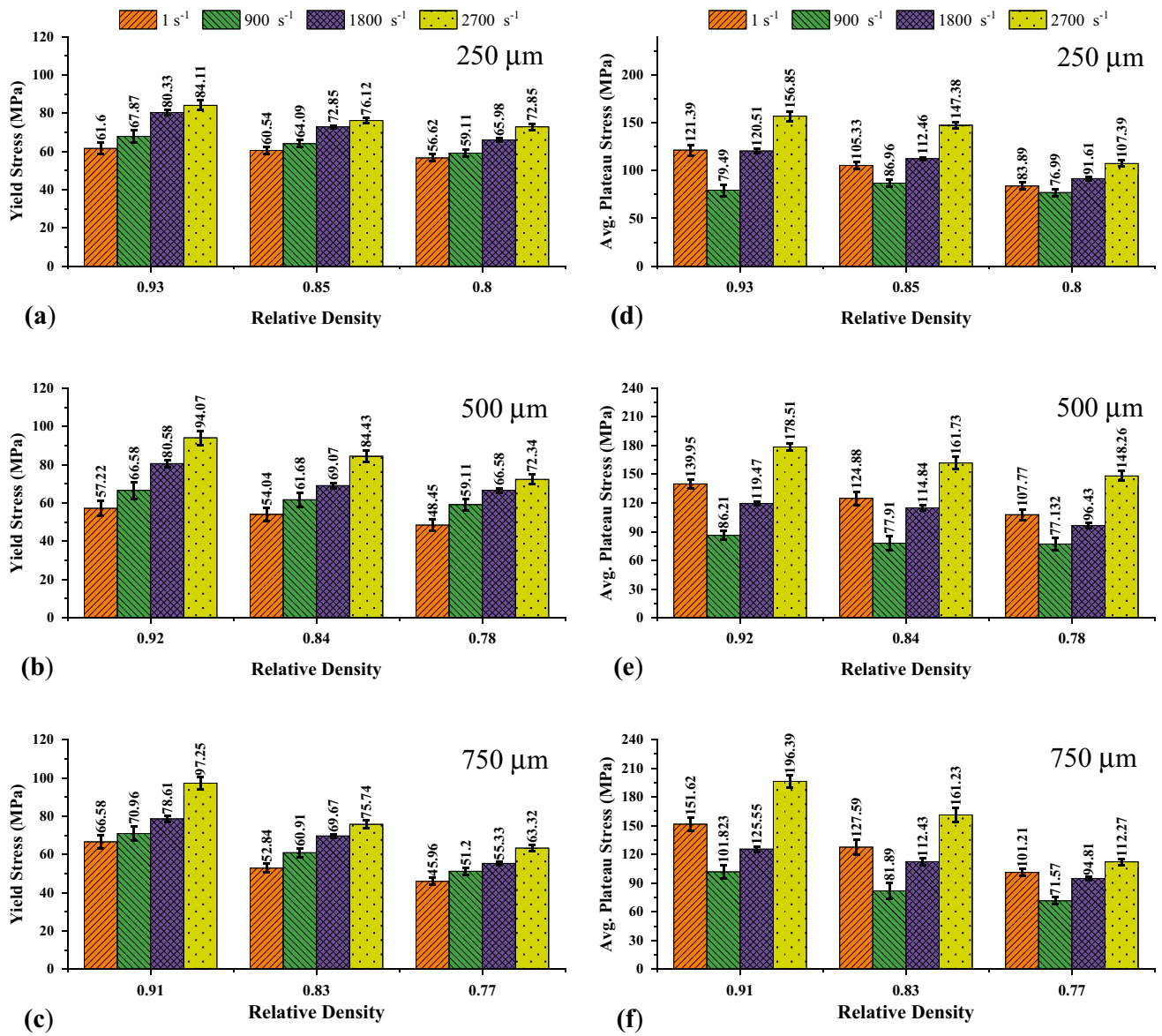
Fig. 6 Compressive properties of AMSFs, including yield stress and average plateau stress of three different sizes: (a, d) − 250 mm, (b, e) − 500 mm, and (c, f) − 750 mm

strain rates (2700 s^{-1}), the hollow particles are fractured entirely due to the brittle nature and the dynamic loading of the material. Also, the material is not entirely dense, and the gap is retained due to particle failure. This deformation behavior of AMSFs is attributed to the amount of plastic flow of the matrix materials, the brittle nature of Al$_2$O$_3$ hollow particles, and sample loading.

4. Discussions

This section presents a detailed discussion of the AMSFs from the viewpoint of hardening, energy absorption, and deformation. The deformation behavior of the samples is explored using the fracture images of the samples tested under high-strain rate conditions. The hardening rate and energy absorption properties are measured in Section 2.3.2.

4.1 Hardening Rate

To probe the hardening behavior of the AMSFs, the derivate of the stress–strain data is calculated and presented in Fig. 8(a), (b), (c), (d), (e), (f), (g), (h), and (i). These curves are plotted to the maximum strain obtained from respective stress–strain data, reported by Xia et al. and others (Ref 16, 28, 31). The initial stage of the HR curves showed a sudden drop representing the linear elastic region of the stress–strain data. Later, a rise in the HR values means the hardening of the material. The data for all the conditions are greater than zero, and this behavior indicates a constant rise in HR without any stress drops. It is observed from Fig. 8 that the HR decreased with an increase in volume fraction and formed a local plateau region for quasi-static tests. The HR behavior is not evident in samples tested at medium strain rates (900 and 1800 s^{-1}). After the initial stage, the curve followed quasi-static behavior. This indicates that the strain hardening in the samples is more significant beyond 1800 s^{-1} across all the samples of AMSFs.
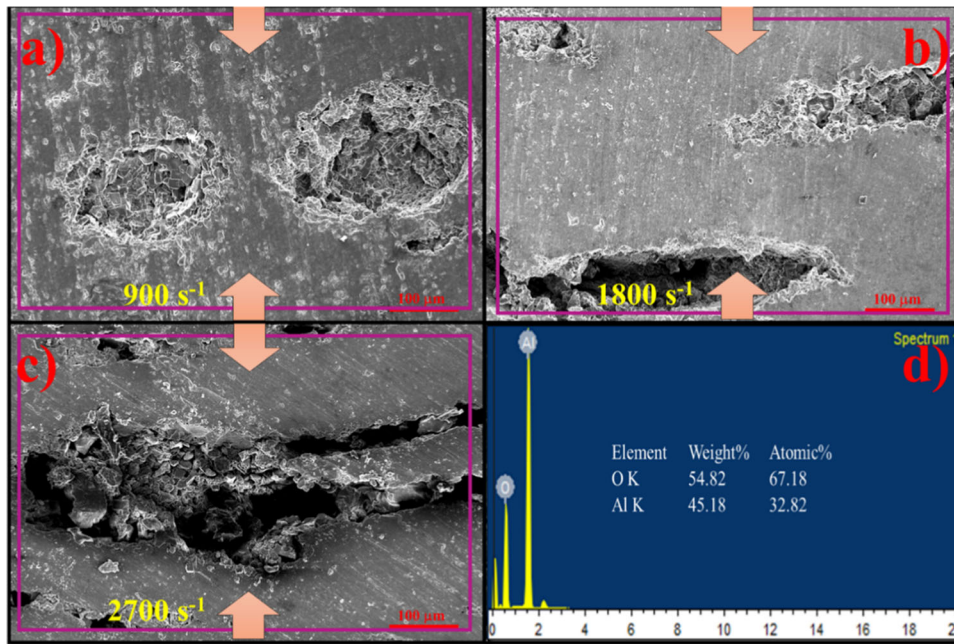
Fig. 7 Representative cross-sectional images of AMSFs sample #3 tested at (a) 900 s^{-1}, (b) 1800 s^{-1}, (c) 2700 s^{-1} strain rates, and (d) the EDX spectrum of (c)

In contrast to low and medium strain rates, the high-strain rate curve continues to increase after the initial drop in HR data. This hardening behavior is significant with an increase in volume fraction. Also, the deviation between the low- and high-strain rates is evident at low densities. For example, the deviation in the low- and high-strain rate data for sample #9 (relative density − 0.77) is higher than in sample #1 (relative density − 0.93). Collectively, the AMSFs have shown the hardening behavior prominently at 2700 s^{-1} strain rates. However, the hardening behavior is not dominant at lower strain rates, which may be attributed to the material's response.

4.2 Energy Absorption Properties

The EA and SEA values for all the samples tested at low- and high-strain rates are shown in Fig. 9(a), (b), (c), (d), (e), (f), (g), (h), and (i), as shown in Section 2.3.3. All the measurements are considered up to 40% strain for assessment purposes, as shown in Table 2. The EA of quasi-static and dynamic tests followed a decrease in trend with relative density. The maximum EA and SEA data at low- and high-strain rates are 52.76 MJ/m^3 and 21.47 kJ/kg and 69.90 MJ/m^3 and 28.45 kJ/kg (Sample #7), respectively. Similarly, with an increase in the volume fraction of the particles, the energy absorption decreases for different sizes of hollow particles. This suggests that the volume fraction of the particles shows the minimum effect on energy absorption. But, the energy absorption rises with the increase in particle size. It is observed that, at 40% strain, the EA and SEA data of AMSFs showed better performance under dynamic loading. This behavior suggests that the AMSF performance is superior under dynamic loading (2700 s^{-1}). However, further analysis is required to understand the overall performance of the samples.

The I-EAE data provide the maximum mechanical energy; the sample absorbs under large deformation. The I-EAE values in Table 2 are obtained by taking mean values between the 5% and 40% strain data (plateau region). In general, the efficiency of a material is based on the slope of the stress–strain curve in the plateau region (Ref 11). The lower the slope of the curve, the higher the efficiency. Figure 5 qualitatively suggests that the particles of smaller diameters and high-volume fractions may have more efficiency due to the less hardening in the plateau region. Also, the efficiency trend of all the size ranges increases in terms of volume fraction. This trend is prominently observed in SFs with small particles.

Under dynamic loading, the maximum strain attained is less than the sample's densification strain. As shown in Fig. 16 in Appendix, the EAC is considered at 40% strain, as explained in the previous section. Compared to static tests for low-volume fractions, the EAC data have increased under dynamic loading. However, the results are not encouraging for higher volume fractions. There is a drop in EAC values for all the size ranges. This behavior can be attributed to the catastrophic failure of the alumina ceramic hollow particles under dynamic loading. This behavior may also lead to the structural failure of these samples.

The ideal energy absorption data as shown in Table 2 of the AMSFs are encouraging up on its counterpart (quasi-static condition). There is no significant drop in the absorption efficiency, even at a high-strain rate (2700 s^{-1}). The overall energy absorption has improved since there is an improvement in the yield stress data followed by a smooth transition to the plateau region without any stress drops during the deformation. Also, it is observed that concerning the volume fraction of the particles, there is a rise in the I-EAE for both quasi-static and at

a high-strain rate. This accounts for the significant role of the volume fraction irrespective of the particle size. Maximum efficiency is attained at higher volume fractions, attributed to the particles' volume fraction and their uniform deformation without significant stress drops. This may account for the reduction in the slope of the stress–strain curve and the increase in the overall absorption energy. The EA data of previous studies on aluminum matrix syntactic under different loading conditions against the current study are compared in Fig. 10. The data show that the AMSFs have outperformed some literature data under quasi-static and dynamic loadings. Also, the energy absorption properties have shown enhancement compared to the earlier literature works as shown in Fig. 10. This behavior may be attributed to the processing route and the microsize alumina reinforcements.

4.3 Compressive Behavior

The energy absorption capacity and energy absorption efficiency properties are discussed in the earlier sections. These properties are essential to designing a material based on the maximum expected efficiency and absorption capacity. The correlation between the energy absorption properties and the stress needs to be further analyzed to achieve a suitable porosity at a specific stress level. The results displayed in Fig. 11(a) and (b) on a logarithmic normalized scale are energy absorption capacity versus stress for quasi-static and high-strain rate data. The E_{Al} is the modulus of the matrix material (aluminum). Also, the normalized EAC versus stress data can be divided into three regions similar to the stress–strain curve of cellular material, as shown in Fig. 11(a) (Ref 39). A linear elastic region (A) is where the mechanical energy is absorbed in bending and displacing the hollow particles inside the matrix. In plateau (B), the region dissipates energy to fracture the hollow particles and fill the newly evolved voids. In the later part, the material is a fully dense composite with no traces of pours inside the matrix. The densification point is termed the 'shoulder point' by Zhang et al., which is at the densification point (Ref 40). At this point, the cellular materials tend to
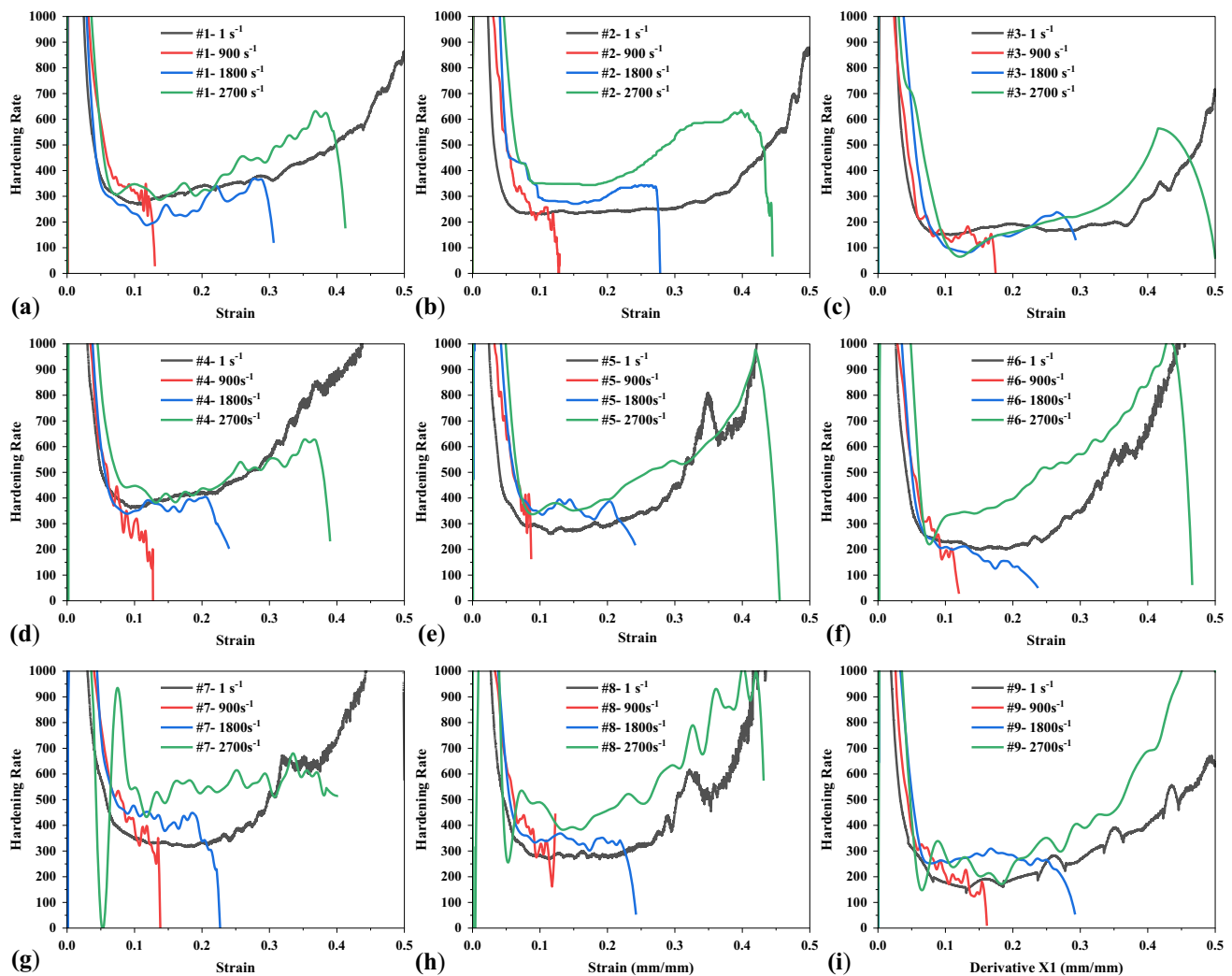

Fig. 8 Hardening rate versus strain of different sample IDs (a) #1, (b) #2, (c) #3, (d) #4, (e) #5, (f) #6, (g) #7, (h) #8, and (i) #9
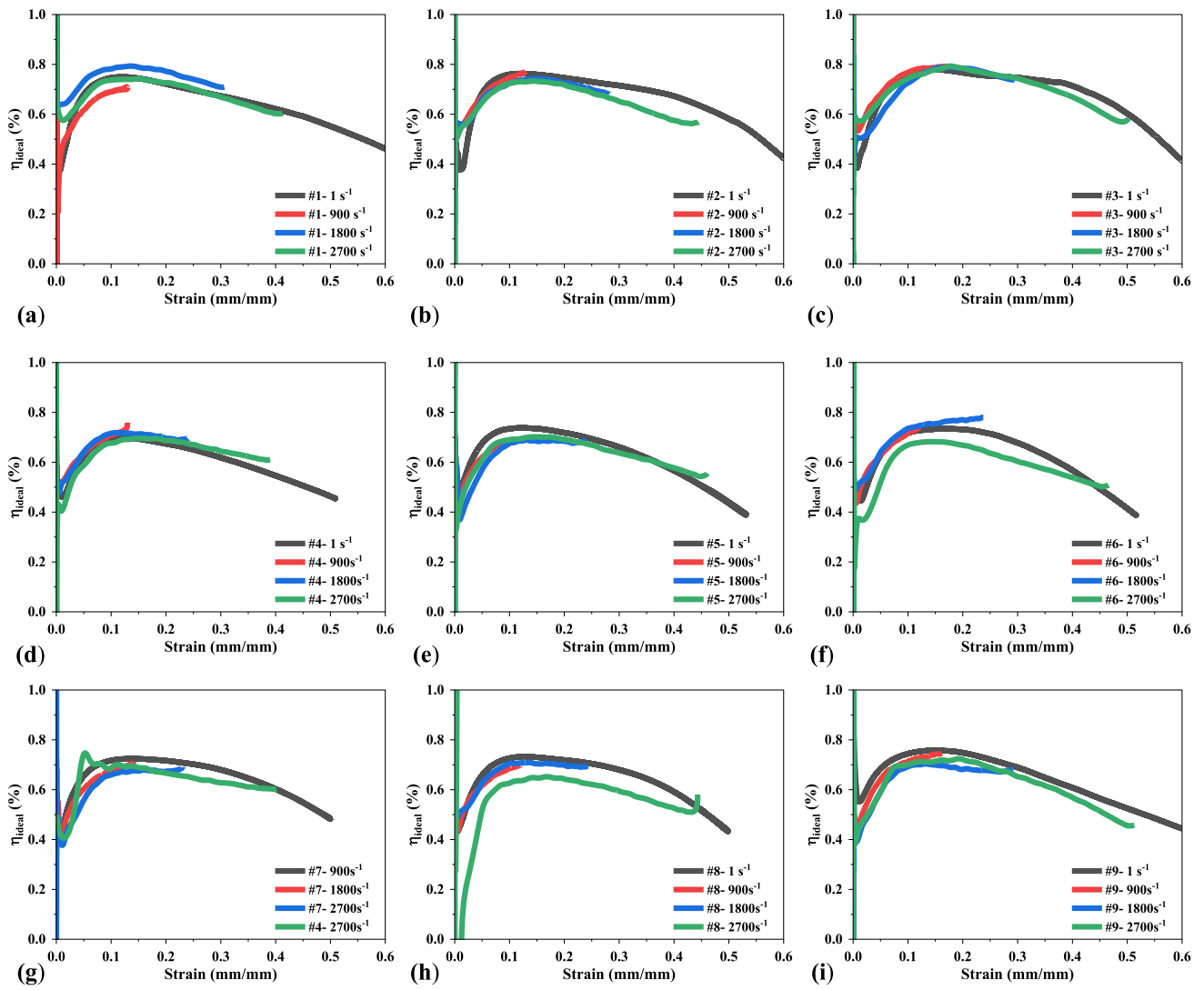
Fig. 9 Energy absorption efficiency of sample IDs: (a) #1, (b) #2, (c) #3, (d) #4, (e) #5, (f) #6, (g) #7, (h) #8, and (i) #9

Table 2 Material properties of Al-matrix syntactic foams tested under compression

| Sample ID	Relative density	Quasi-static, 1 s^{-1}				High-strain rate, 2700 s^{-1}			
		EA (MJ/m^3) at 0.4 strain	SEA (kJ/kg) at 0.4 strain	Densification strain	η_{ideal}, %	W (MJ/m^3) at 0.4 strain	SEA (kJ/kg) at 0.4 strain	Maximum strain	η_{ideal}, %
#1	0.93	45.22	18.00	0.52	69.37	56.53	22.51	0.41	67.47
#2	0.85	38.99	16.98	0.54	70.61	54.32	23.67	0.45	68.78
#3	0.80	31.98	14.80	0.55	72.34	40.70	18.84	0.50	78.92
#4	0.92	50.72	20.41	0.50	63.56	62.09	25.00	0.44	62.27
#5	0.84	42.58	18.77	0.50	66.40	59.32	26.16	0.40	65.52
#6	0.78	35.64	16.92	0.51	66.56	53.06	25.19	0.46	65.66
#7	0.91	52.76	21.47	0.49	67.95	69.90	28.45	0.44	60.11
#8	0.83	44.33	19.78	0.50	67.63	56.93	25.40	0.39	65.01
#9	0.77	30.31	14.57	0.50	69.74	41.89	20.15	0.46	67.04
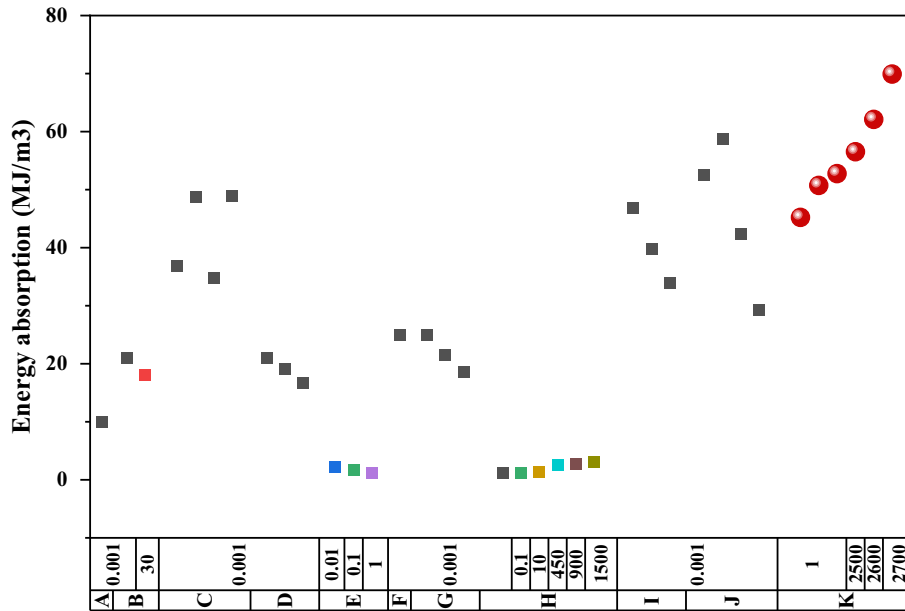
Fig. 10 Energy absorption (MJ/m^3) properties of present work (K) compared against literature data tested at different relative density and strain rates [Literature: A-(Ref 32), B-(Ref 33), C-(Ref 7), D-(Ref 30), E-(Ref 34), F-(Ref 35), G-(Ref 36), H-(Ref 37), I-(Ref 38), and J-(Ref 11)]

absorb maximum energy. Later, the W/E_{Al} versus σ/E_{Al} curve becomes horizontal. Also, during the plateau region, the energy absorption is nearly constant. This study considers the shoulder point at 40% strain before the densification strain for evaluation purposes. Therefore, the normalized EAC versus stress data summary is at 40% data.

In Fig. 11(c), the shoulder points of quasi-static and high-strain rate data are shown for different densities obtained from the various combinations of size and volume fractions. The data show a linear rise in the W/E_{Al} value with an increase in the σ/E_{Al} in both testing conditions. However, a notable offset is observed in the high-strain rate data. For example, for a known value of σ/E_{Al} (0.003), the energy absorption value for quasi-static and dynamic testing is 6.78×10^{-4} and 7.31×10^{-4}. The slope of the linear fit curve for different shoulder points considered from Fig. 11(a) and (b) and its intercept indicates the energy absorption capacity of AMSFs. This behavior suggests that the AMSFs showed better energy absorption properties at high-strain rate conditions with maximum. W/E_{Al} value at a given σ/E_{Al}. Further, the mathematical expression for the shoulder point for different test conditions is shown in Table 3. These expressions are useful when designing a material with optimum energy absorption for a given test condition.

4.4 Deformation Behavior

Figure 12(a), (b), and (c) displays the DIC analysis for three strain rates (900, 1800, and 2700 s^{-1}) captured from the high-speed images, respectively. These images are arranged based on the strain data for each test. A uniform deformation is observed in the samples tested at all strain rates up to the elastic limit. Also, during the shift from the elastic to the plastic stage, the deformation gradient as shown in Fig. 12 is uniform. This behavior agrees with the stress–strain response from Fig. 5. Further, up to the 1800 s^{-1}, the material response is almost uniform. At a strain rate of 2700 s^{-1}, a significant distortion is observed after 0.2 strain. This behavior is attributed to the plastic flow of the matrix material due to cracking and fracture of the external surface of the samples. Also, it is observed that the DIC analysis failed to capture the significant distortion in the sample under compression after 0.2% strain.

Further, Fig. 13(a) and (b) shows the fractured samples of different particle sizes and volume fractions tested at low- and high-strain rates. In Fig. 13(b), the quasi-static test samples are deformed up to 60% strain. The fractured samples showed a minimum structural failure in all conditions. The failure initiates from the external surface due to the presence of a large number of unconfined hollow particles with matrix material. However, the confined particles inside the matrix tend to fracture and contribute to the densification of the material.
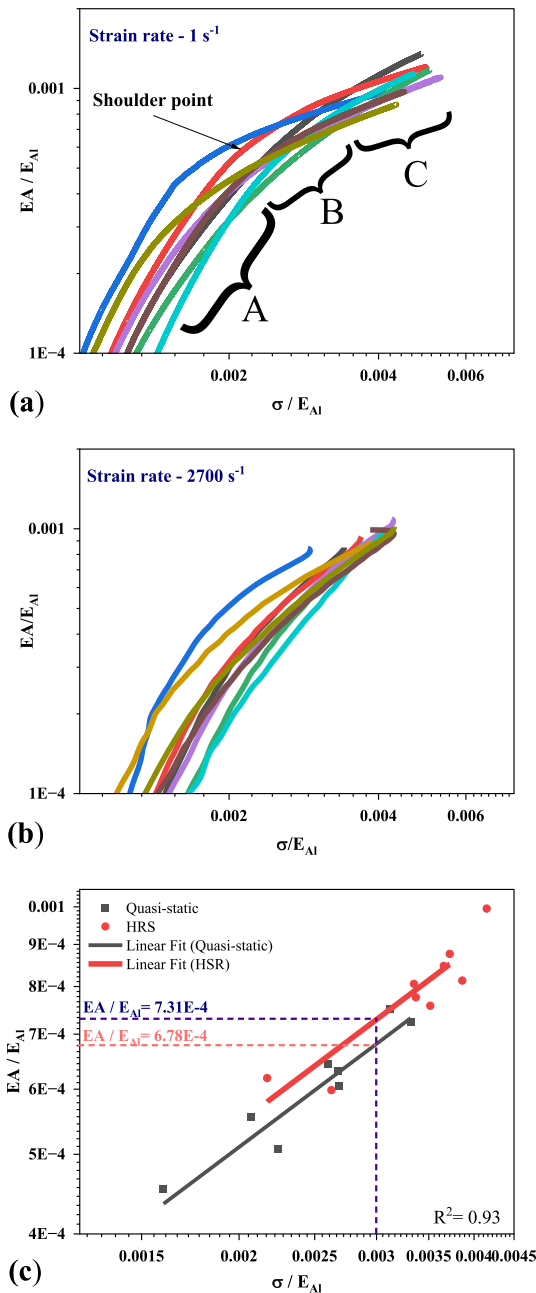
These cracks extended further along the lateral direction to accommodate the external force, which resulted in random cracks along the surface of the samples. The appearance of such typical plastic deformation was due to the complete densification of the AMSFs.

In contrast to the low-strain rate behavior, many cracks are observed during high-strain rate tests deformed up to 40-50% strain. Also, the samples' surface is significantly affected, and structural failures are observed in samples with hollow particles above 20% volume fraction. This behavior is observed due to the reduced matrix percentage and rapid crack propagation due to the impact, which results in the hardening of AMSFs. Another factor affecting the hardening and delamination is matrix failure at the interface of two hollow particles. Figure 14 shows the representative fracture images of samples tested at low- and high-strain rates. Based on observation of the cross-section of the samples, during quasi-static deformation, the hollow particles fractured during the deformation, and the matrix material buckled at the interface of the two particles. This behavior helps in more plateau slop during the hardening. However, the matrix interface fractured and failed during the dynamic loading before attaining the densification zone, as shown in Fig. 14(b).

Thus, during quasi-static deformation, the hollow particles and matrix material compensate for the energy absorption in the form of uniform particle failure and the plastic flow of the matrix. During high-strain rates, they show hardening behavior due to the matrix failure at the interface after the failure of the hollow particles.

5. Conclusions

This work presents the behavior of alumina hollow particle-reinforced aluminum matrix syntactic foams at different strain rates. The following are the conclusions drawn from this work:

1. The aluminum matrix syntactic foams with different densities ranging from 2.52 to 2.09 g/cm^3 are produced using the hot compression technique with densities close to the theoretical values.
2. A series of mechanical studies performed at different strain rates showed enhanced mechanical properties over literature. The AMSF performed better up to a strain rate of 2700 s^{-1} with a maximum strain range of 40-45%.
3. A significant deviation is observed in the hardening behavior of the AMSFs with different densities. Also, up to 1800 s^{-1}, the hardening behavior is not evident in AMSFs.
4. There is no significant drop in the energy absorption properties of the AMSFs at high-strain rates. The energy absorption efficiency of AMSFs has shown a maximum value of 72.34 and 78.92% for low- and high-strain rates, respectively.
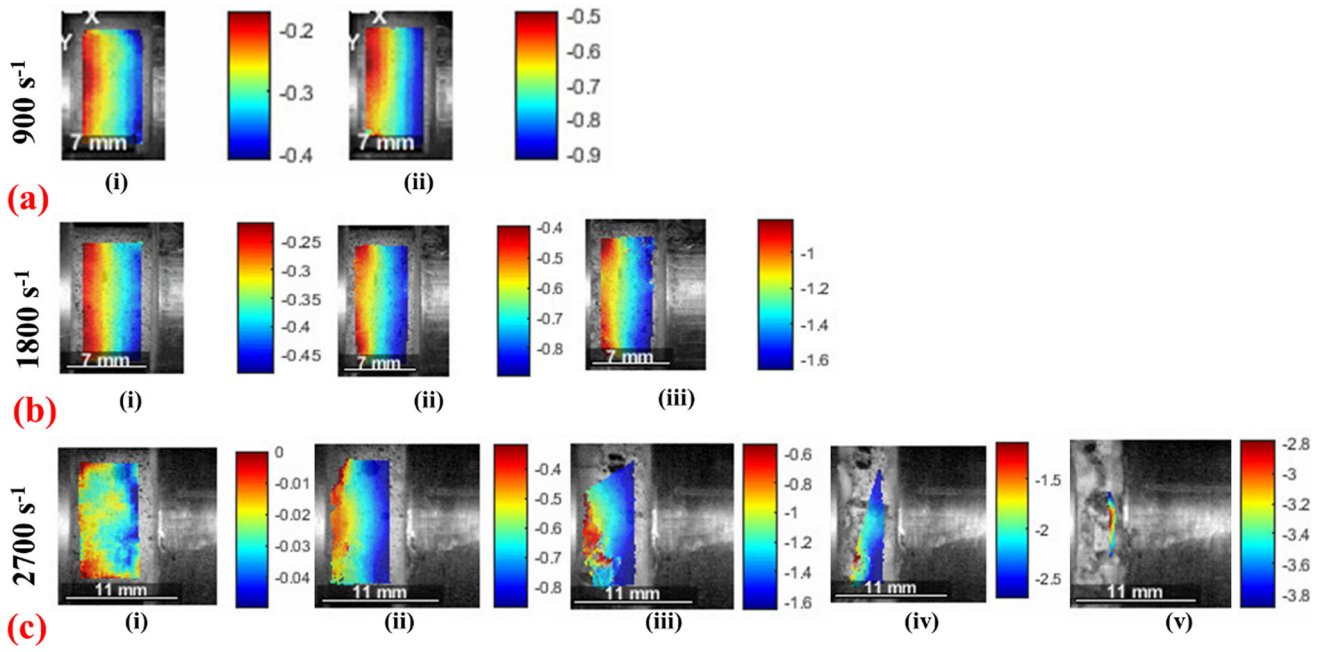
Fig. 11 Energy absorption diagram for (a) quasi-static, (b) high-strain rate studies, and (c) a summary of the data at 40% strain for A and B

Table 3 Mathematical expression for different conditions

Condition	Mathematical expression of the shoulder point
Quasi-static	$log\frac{W}{E_{Al}} = 0.71 log\frac{\sigma}{E_{Al}} - 1.37$
High-strain rate	$log\frac{W}{E_{Al}} = 0.72 log\frac{\sigma}{E_{Al}} - 1.33$

Fig. 12 Deformation process of AMSFs at three strain rates (a) − 900 s^{-1}, (b) − 1800 s^{-1}, and (c) − 2700 s^{-1} from DIC analysis with the axial displacement field captured at different strains (i) 0.005, (ii) 0.1, (iii) 0.2, (iv) 0.31, and (v) 0.475
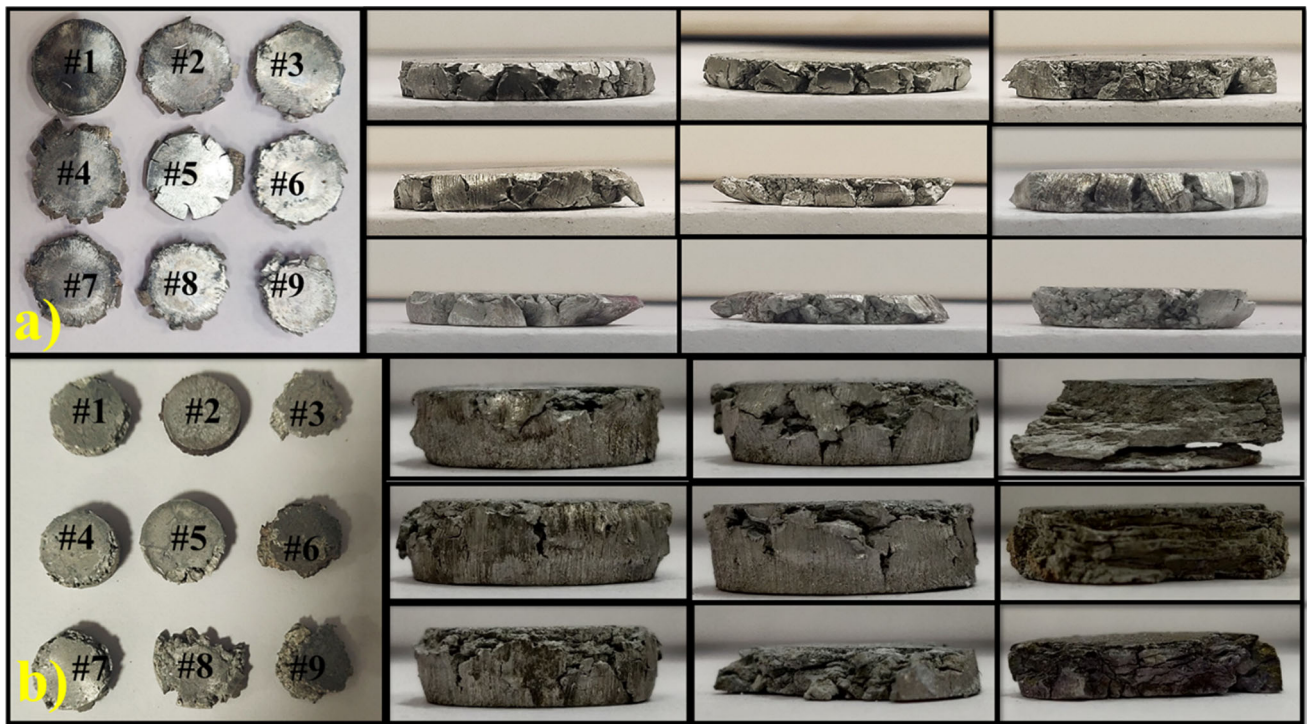

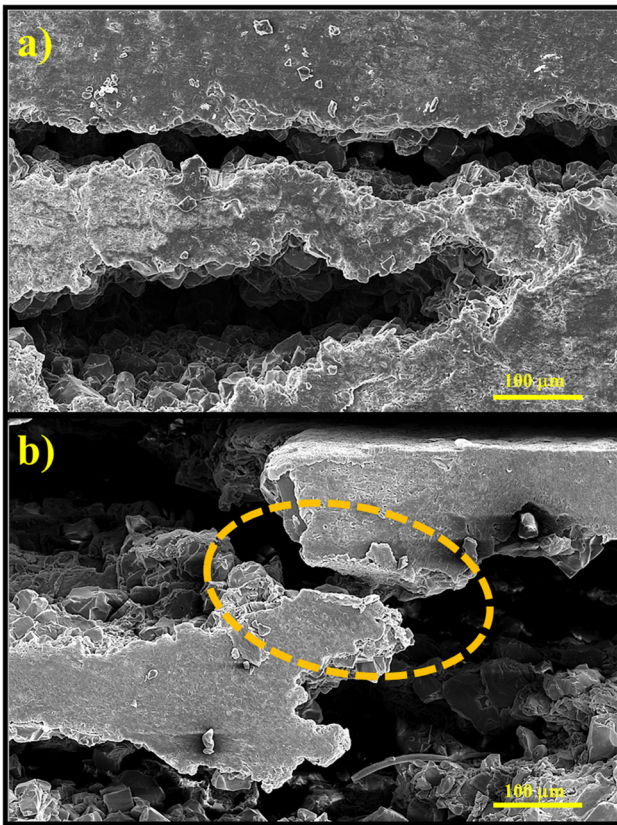**Fig. 13** Representative deformed samples tested at (a) 1 s^{-1} and (b) 2700 s^{-1}

5. The fracture studies suggest a random crack growth during quasi-static deformation. During dynamic loading, the matrix interface suffers premature densification, contributing to the hardening of AMSFs.

The mechanical properties and deformation response of the AMSFs are conducted, facilitating the energy absorption properties. In addition, AMSFs show enhanced properties, stiffness, and stability during dynamic loadings, making them suitable for various applications in fields such as automotive, aerospace, and defensive engineering.

However, this work has been limited to different strain rates at room temperatures. For future studies, the dynamic nature of the AMSFs at different temperatures and their energy absorption properties needs to be understood. These studies are promising in exploring the material response under various environmental conditions.

Data availability

The raw/processed data required shall be produced on request, as the current work submitted is a part of ongoing research.
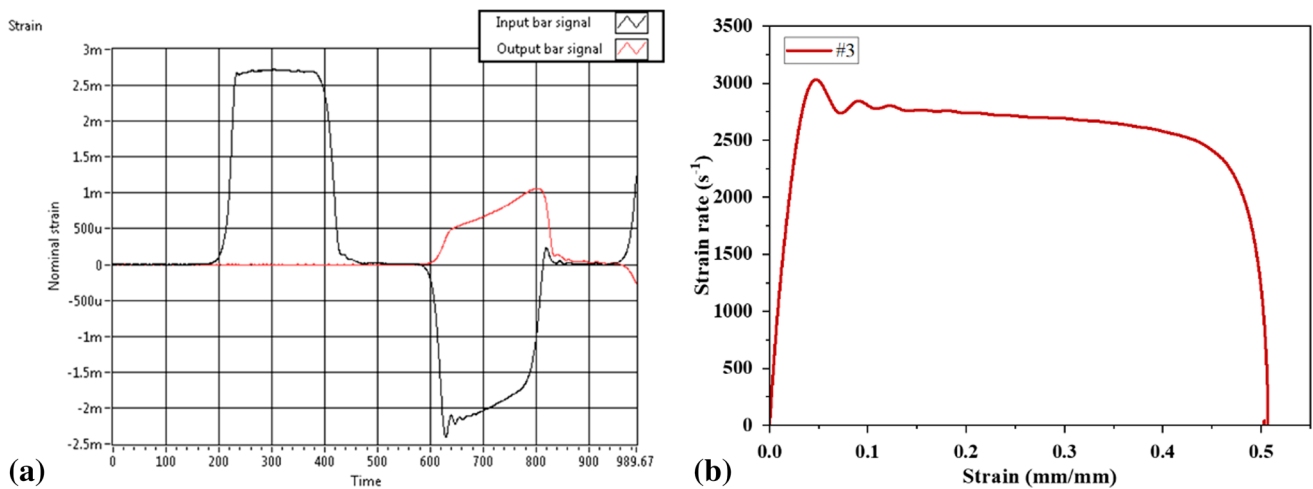

Fig. 14 Cross-sectional images of sample #9 tested at (a) quasi-static and (b) dynamic conditions

Fig. 15 The raw data and the strain versus strain rate data from the SHPB studies for sample #3
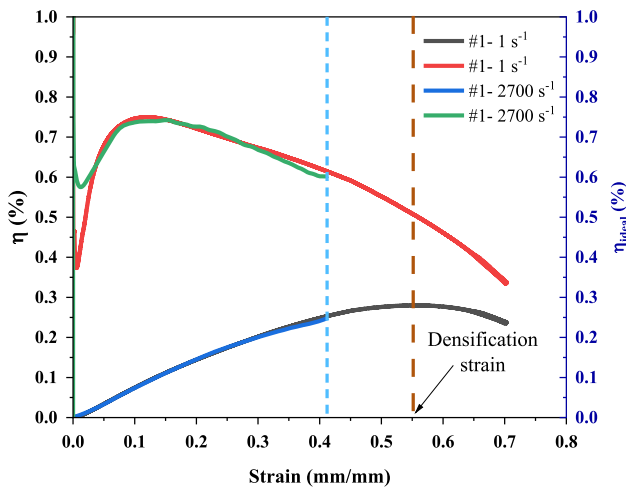
Fig. 16 A representative graph showing the densification strain for quasi-static deformation

Appendix

See Figs. 15 and 16.

References

1. L. Zhang and D. Townsend, Strain Rate Dependent Compressive Mechanical Properties and Dynamic Failure of Pre-Strained Epoxy Syntactic Foam, *Compos. A Appl. Sci. Manuf.*, 2023, **165**, 107360
2. K.S.M. Sonti, S. Vincent, and S.K.R. Narala, Quasi-Static Compressive Response and Energy Absorption Properties of Aluminum Matrix Syntactic Foams: Room Temperature and Elevated Temperature Conditions, *Mater. Today Commun.*, 2023, **35**, 105580
3. P. Prabhakar, H. Feng, S.P. Subramaniyan, and M. Doddamani, Densification Mechanics of Polymeric Syntactic Foams, *Compos. B Eng.*, 2022, **232**, 109597
4. B. Zhang, L. Wang, J. Zhang, Y. Jiang, W. Wang, and G. Wu, Deformation and Energy Absorption Properties of Cenosphere/Aluminum Syntactic Foam-Filled Circular Tubes under Lateral Quasi-Static Compression, *Int. J. Mech. Sci.*, 2021, **192**, 106126
5. B. Zhang, J. Zhang, L. Wang, Y. Jiang, W. Wang, and G. Wu, Bending Behavior of Cenosphere Aluminum Matrix Syntactic Foam-Filled Circular Tubes, *Eng. Struct.*, 2021, **243**, 112650
6. K. Sun, L. Wang, Q. Zhang, B. Meng, Z. Wei, H. Su, G. Wei, S.V. Shil'ko, and G. Wu, Preparation and Quasi-Static Compression Properties of Hybrid Aluminum Matrix Syntactic Foam Reinforced with Glass Cenospheres and Silicon Carbide Nanowires, *Mater. Charact.*, 2023, **195**, 112496
7. L. Pan, D. Rao, Y. Yang, J. Qiu, J. Sun, N. Gupta, and Z. Hu, Gravity Casting of Aluminum-Al_2O_3 Hollow Sphere Syntactic Foams for Improved Compressive Properties, *J. Porous Mater.*, 2020, **27**(4), p 1127–1137
8. P.K. Rohatgi, J.K. Kim, N. Gupta, S. Alaraj, and A. Daoud, Compressive Characteristics of A356/Fly Ash Cenosphere Composites Synthesized by Pressure Infiltration Technique, *Compos. A Appl. Sci. Manuf.*, 2006, **37**(3), p 430–437
9. L.P. Zhang and Y.Y. Zhao, Mechanical Response of Al Matrix Syntactic Foams Produced by Pressure Infiltration Casting, *J. Compos. Mater.*, 2007, **41**(17), p 2105–2117
10. C.A. Vogiatzis and S.M. Skolianos, On the Sintering Mechanisms and Microstructure of Aluminium-Ceramic Cenospheres Syntactic Foams Produced by Powder Metallurgy Route, *Compos. A Appl. Sci. Manuf.*, 2016, **82**, p 8–19
11. K.S.M. Sonti, S. Vincent, and S.K.R. Narala, Effect of Single and Hybrid Hollow Sphere Reinforcement on the Deformation Mechanism of Aluminum Matrix Syntactic Foam at a Low Strain Rate, *J. Alloys Compd.*, 2022, **901**, 163573
12. M. Porfiri and N. Gupta, Effect of Volume Fraction and Wall Thickness on the Elastic Properties of Hollow Particle Filled Composites, *Compos. B Eng.*, 2009, **40**(2), p 166–173
13. N. Gupta, C.S. Karthikeyan, S. Sankaran, and Kishore, Correlation of Processing Methodology to the Physical and Mechanical Properties of Syntactic Foams With and Without Fibers, *Mater. Charact.*, 1999, **43**(4), p 271–277
14. I.N. Orbulov, A. Kemény, Á. Filep, and Z. Gácsi, Compressive Characteristics of Bimodal Aluminium Matrix Syntactic Foams, *Compos. A Appl. Sci. Manuf.*, 2019, **124**, 105479
15. Y. Zhang and Y. Zhao, Hysteretic Energy Dissipation in Aluminium Matrix Syntactic Foam under Intermittent Cyclic Compression, *Materialia*, 2019, **6**, 100286
16. Y. Xia, J. Shi, and Y. Mu, Compressive Behaviour of Open-Cell Al–Si Alloy Foam Produced by Infiltration Casting, *Mater. Sci. Technol.*, 2023, **39**, p 1–13
17. Y. Alvandi-Tabrizi and A. Rabiei, Use of Composite Metal Foam for Improving Absorption of Collision Forces, *Procedia Mater. Sci.*, 2014, **4**, p 377–382
18. Z. Fan, Y. Miao, Z. Wang, B. Zhang, and H. Ma, Effect of the Cenospheres Size and Internally Lateral Constraints on Dynamic Compressive Behavior of Fly Ash Cenospheres Polyurethane Syntactic Foams, *Compos. B Eng.*, 2019, **171**, p 329–338
19. M.D. Goel, V. Parameswaran, and D.P. Mondal, High Strain Rate Response of Cenosphere-Filled Aluminum Alloy Syntactic Foam, *J. Mater. Eng. Perform.*, 2019, **28**(8), p 4731–4739
20. D.K. Balch, J.G. O'Dwyer, G.R. Davis, C.M. Cady, G.T. Gray, and D.C. Dunand, Plasticity and Damage in Aluminum Syntactic Foams Deformed under Dynamic and Quasi-Static Conditions, *Mater. Sci. Eng., A*, 2005, **391**(1), p 408–417
21. D.D. Luong, O.M. Strbik, V.H. Hammond, N. Gupta, and K. Cho, Development of High Performance Lightweight Aluminum Alloy/SiC Hollow Sphere Syntactic Foams and Compressive Characterization at Quasi-Static and High Strain Rates, *J. Alloys Compd.*, 2013, **550**, p 412–422
22. S. Broxtermann, M. Vesenjak, L. Krstulović-Opara, and T. Fiedler, Quasi Static and Dynamic Compression of Zinc Syntactic Foams, *J. Alloys Compd.*, 2018, **768**, p 962–969
23. X. Liang, H. Luo, Y. Mu, M. Chen, J. Ye, and D. Chi, Quasi-Static and Dynamic Compression of Aluminum Foam at Different Temperatures, *J. Mater. Eng. Perform.*, 2019, **28**(8), p 4952–4963
24. Q. Zhang, Y. Lin, H. Chi, J. Chang, and G. Wu, Quasi-Static and Dynamic Compression Behavior of Glass Cenospheres/5A03 Syntactic Foam and Its Sandwich Structure, *Compos. Struct.*, 2018, **183**, p 499–509
25. M.A. Meyers, *Dynamic Behavior of Materials*, Wiley, Hoboken, 1994
26. K.P. Dharmasena, H.N.G. Wadley, Z. Xue, and J.W. Hutchinson, Mechanical Response of Metallic Honeycomb Sandwich Panel Structures to High-Intensity Dynamic Loading, *Int. J. Impact Eng.*, 2008, **35**(9), p 1063–1074
27. K.S.M. Sonti, B. Dash, K.V. Vamsi, H. Bandyopadhyay, B. Ravisankar, K. Sivaprasad, and S. Karthikeyan, Deformation Behavior of Al/Cu in-Situ Metal-Intermetallic Laminates at Low and High Strain Rates, *J. Alloys Compd.*, 2021, **873**, 159767
28. N.I. Vazquez-Fernandez, G.C. Soares, J.L. Smith, J.D. Seidt, M. Isakov, A. Gilat, V.T. Kuokkala, and M. Hokka, Adiabatic Heating of Austenitic Stainless Steels at Different Strain Rates, *J. Dyn. Behav. Mater.*, 2019, **5**(3), p 221–229
29. K.S.M. Sonti, S. Vincent, and S.K.R. Narala, Effect of Single and Hybrid Hollow Sphere Reinforcement on the Deformation Mechanism of Aluminum Matrix Syntactic Foam at a Low Strain Rate, *J. Alloys Compd.*, 2022, **901**, 163573
30. M. Su, H. Wang, H. Hao, and T. Fiedler, Compressive Properties of Expanded Glass and Alumina Hollow Spheres Hybrid Reinforced Aluminum Matrix Syntactic Foams, *J. Alloys Compd.*, 2020, **821**, 153233
31. S.S. Gvk, M.J. Tan, and Z. Liu, Analysis of Strain Rate Sensitivity and Strain Rate Hardening in Co–Cr–Ni–Mo Wires Drawn with Different Drawing Practices, *Met. Mater. Int.*, 2019, **25**(4), p 1047–1062
32. B. Leveles, A. Kemény, and A. Szijártó, Mechanical Investigation of In-Situ Produced Aluminium Matrix Syntactic Foam-Filled Tubes, *Mater. Today Proc.*, 2021 https://doi.org/10.1016/j.matpr.2020.12.161

33. N. Movahedi, M. Vesenjak, L. Krstulović-Opara, I.V. Belova, G.E. Murch, and T. Fiedler, Dynamic Compression of Functionally-Graded Metal Syntactic Foams, *Compos. Struct.*, 2021, **261**, 113308

34. M. Mohbe, D.M. Afzal Khan, and D.P. Mondal, Microstructural Characterization and Deformation Behavior of Zn–8Al-Cenosphere Hybrid Foam, *Trans. Indian Inst. Met.*, 2019, **72**(9), p 2477–2486

35. K. Al-Sahlani, E. Kisi, and T. Fiedler, Impact of Particle Strength and Matrix Ductility on the Deformation Mechanism of Metallic Syntactic Foam, *J. Alloys Compd.*, 2019, **786**, p 292–299

36. M. Su, H. Wang, and H. Hao, Compressive Properties of Aluminum Matrix Syntactic Foams Prepared by Stir Casting Method, *Adv. Eng. Mater.*, 2019, **21**(8), p 1900183

37. D. Muchhala, B.N. Yadav, A. Pandey, V. Chilla, MMd. Shafeeq, G. Gupta, S. Sathaiah, and D.P. Mondal, Influences of Relative Density and Strain Rate on the Mechanical Properties of Al-Cenosphere-SWNTs Hybrid Foams, *Int. J. Mech. Sci.*, 2021, **198**, 106388

38. J.A. Santa Maria, B.F. Schultz, J.B. Ferguson, and P.K. Rohatgi, Al–Al_2O_3 Syntactic Foams—Part I: Effect of Matrix Strength and Hollow Sphere Size on the Quasi-Static Properties of Al-A206/Al_2O_3 Syntactic Foams, *Mater. Sci. Eng. A*, 2013, **582**, p 415–422

39. J. Wang, A. Liu, Q. Ao, C. Wu, J. Ma, and P. Cao, Energy Absorption Characteristics and Preparation of Porous Titanium with High Porosity, *Mater. Today Commun.*, 2023, **34**, 105003

40. H. Zhang, H. Zhou, Z. Zhou, H. Zeng, X. Zhang, J. Yang, H. Lei, and F. Han, Energy Absorption Diagram Characteristic of Metallic Self-Supporting 3D Lattices Fabricated by Additive Manufacturing and Design Method of Energy Absorption Structure, *Int. J. Solids Struct.*, 2021, **226–227**, 111082